nature communications

Article

https://doi.org/10.1038/s41467-026-76899-1

Gentle yet powerful artificial muscles enabled by hierarchical structure engineering

Received: 17 February 2026

Accepted: 7 August 2026

Published online: 19 August 2026

Check for updates

Han Liu[1], Baohu Wu[2], Lei Hou[1] ✉ & Peiyi Wu[1] ✉

Developing artificial muscles with simultaneous high actuation performance and mild activation conditions is highly needed but still challenging. Here we broke the limitations through a hierarchical structure design of a dual-stimuli-responsive shape memory polymer (SMP) network, achieved by integrating a double-tail quaternary ammonium surfactant with poly(acrylic acid) via ionic complexation. Notably, the double-tail surfactant exhibits a phase transition around 42 °C, enabling the mild-temperature-triggered actuation. The SMP-based artificial muscle features a hierarchically nanophase-separated structure, consisting of water-responsive hydrophilic PAA domains and thermally responsive hydrophobic PAA/surfactant complex crystalline domains, thus decoupling the actuation stress and strain by different stimuli. The nanostructured artificial muscle achieves an actuation stress of up to 6.4 MPa (isometric) and an actuation strain of up to 79% (load-free), both under heating to ~42 °C, surpassing most existing actuators. Furthermore, the system exhibits self-reversible, force-free cyclic actuation. Our work offers a viable route for multi-scale structural engineering toward high-performance soft actuators.

Artificial muscles, which replicate the directional contraction and relaxation functions of skeletal muscle[1], hold great potential to revolutionize fields such as soft robotics[2], smart textiles[3], and prosthetic devices[4]. Among various actuation systems, stimuli-responsive polymers, including shape memory polymers (SMPs)[5,6], liquid crystal elastomers[7], and dielectric elastomers[8], are particularly attractive due to their light weight, ease of processing, and most notably, their ability to operate without external power sources or pumping components. Significant research efforts have thus been directed toward enhancing key actuation performance metrics[9] such as contractile stress, strain, and work capacity. As a result, many reported artificial muscle systems now surpass the performance benchmarks of natural mammalian skeletal muscle in several aspects[10–12]. In addition to performance, however, the practicality of artificial muscles in real-world applications also depends on the mildness of the stimuli required for activation. For example, in human-robot interaction scenarios[13], the triggering stimulus must be both safe and tolerable for direct contact with the human body. Nevertheless, achieving high actuation performance under such mild conditions remains a major challenge. Dielectric elastomers, for instance, offer high force output and fast response but require high operating voltages, raising safety concerns[14]. Liquid crystal elastomers can undergo large, reversible deformations through thermotropic phase transitions, yet their typically high transition temperatures and limited contractile stresses restrict their applicability[15,16]. Similarly, twisted fiber-based artificial muscles made from nylon[17], polyethylene[18], or aramid[19] can achieve significant contraction only at elevated temperatures, often exceeding 100 °C. Therefore, the development of artificial muscles that combine high actuation performance with mild activation conditions represents a critical and ongoing research challenge.

SMPs have garnered considerable interest for artificial muscle applications due to their unique ability to recover a permanent shape

[1]State Key Laboratory of Advanced Fiber Materials, College of Chemistry and Chemical Engineering, Donghua University, Shanghai, China. [2]Jülich Centre for Neutron Science (JCNS) at Heinz Maier-Leibnitz Zentrum (MLZ) Forschungszentrum Jülich, Garching, Germany. ✉e-mail: houlei@dhu.edu.cn; wupeiyi@dhu.edu.cn

from a programmed temporary one upon stimulation[20,21]. A key advantage lies in their compatibility with diverse external triggers, such as heat[22], light[23], and solvents[24], enabling versatile actuation control. Moreover, SMPs exhibit broadly tunable mechanical properties, making them highly adaptable for customized designs[25]. These characteristics position SMPs as promising candidates for developing artificial muscles that combine high actuation performance with mild activation conditions through rational structural engineering. To realize this potential, two major challenges must be addressed. First, achieving both high actuation stress and high actuation strain remains difficult. The actuation stress in SMPs originates primarily from the release of stored entropic energy within the polymer network, which is governed by the density and strength of junctions (crosslinks or entanglements)[26]. In entangled networks, the achievable stress is constrained by the entanglement plateau modulus (typically around ~1 MPa)[27], as the junction density is fixed by the polymer's entanglement molecular weight. While increasing crosslink density and strength can enhance stress, it often compromises stretchability, thereby reducing actuation strain[28]. Second, conventional SMPs typically exhibit one-way shape memory behavior, lacking intrinsic reversibility. Cyclic actuation usually requires external reprogramming after each recovery step[11]. Although two-way reversible SMPs can achieve reversible actuation under specific external stimuli, sustaining this reversibility typically requires intricate structural design or demonstrates limited actuation performance[29,30]. To overcome this, multi-stimuli responsive SMPs offer a promising alternative. Such systems allow decoupling of actuation stress and strain under different stimuli. Furthermore, the introduction of a second stimulus can enable reprogramming without mechanical intervention, paving the way for fully reversible, self-sufficient actuation cycles.

In this work, we present high-performance artificial muscles based on hierarchically structured SMPs, which achieve forceful actuation under mild conditions and enable external force-free cyclic operation (Fig. 1). The developed SMP features a phase-separated structure, comprising a hydrophilic phase of poly(acrylic acid) (PAA) chains and a hydrophobic phase of ionically complexed PAA with a lamellar-self-assembling, crystallizable double-tail surfactant. The crystallization-melting transition of the surfactant within the hydrophobic domain provides a mild thermal trigger for shape memory. Simultaneously, the hydrogen-bonded PAA network in the hydrophilic phase is water-responsive, forming a highly stretchable hydrogel upon swelling. This allows the SMP to be readily programmed into a highly oriented state with the aid of water. In the dry state, the material exhibits high actuation stress due to strong, high-density ionic crosslinking. In the hydrated state, it demonstrates high actuation strain owing to its exceptional stretchability. Consequently, actuation stress and strain are effectively decoupled by different stimuli, yielding 6.4 MPa stress (isometric) and 79% strain (load-free) under heating to ~42 °C, surpassing most existing artificial muscles. Moreover, the incorporation

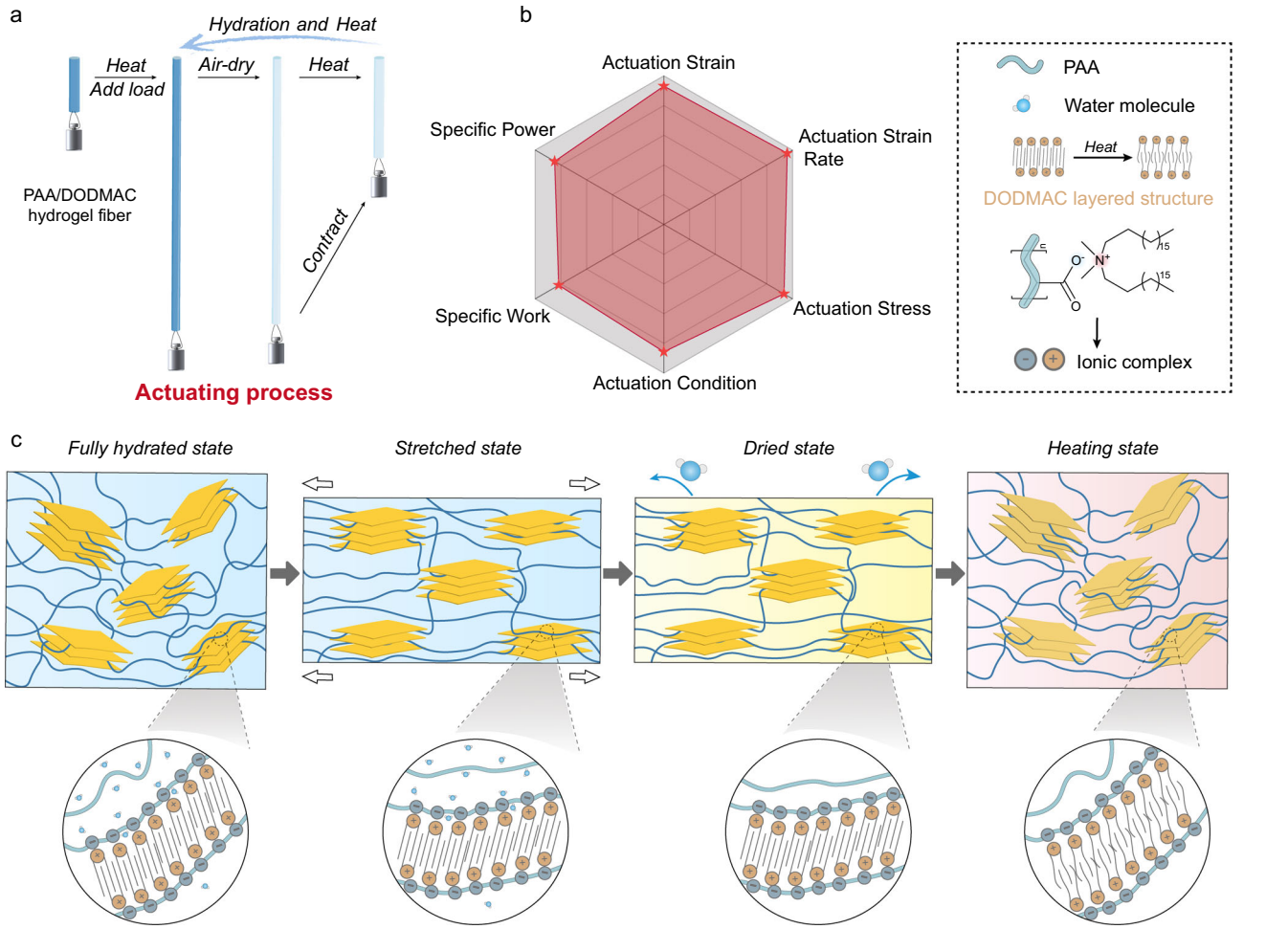


Fig. 1 | Molecular design and actuation mechanism of the artificial muscle. **a** The reversible actuation process of PAA/DODMAC complex fiber. **b** Key advantages of the artificial muscle. **c** Mechanism of water-assisted heat-induced actuation. Under water and thermal stimuli, the artificial muscle demonstrates reversible actuation without external force. The DODMAC-rich phase facilitates a low temperature-induced phase transition within hydrophobic microdomains, offering a mild thermal pathway for shape programming and recovery.

of water responsiveness enables excellent self-reversible actuation without external force.

Results

Preparation of the artificial muscle and its water-responsive behavior

The artificial muscle is based on a supramolecular complex system of hydrophilic polyelectrolyte (PAA) and a double-tail quaternary ammonium surfactant (dioctadecyl dimethyl ammonium chloride, DODMAC). We choose the amphiphilic DODMAC mainly from two aspects: (i) its positively charged quaternary ammonium groups can form strong ionic complexes with the negatively charged carboxylate groups of PAA, generating dense physical crosslinks; and (ii) DODMAC self-assembles into bilayer lamellar structures and exhibits a distinct thermally induced order-disorder transition around 45 °C, where its alkyl chains reversibly transform between a highly ordered crystalline state and a disordered liquid-like phase, thereby offering a mild thermal trigger for actuation[31–33]. Polymerizing AA with the presence of DODMAC bilayer lamellas in an aqueous solution followed by incubated in water to the equilibrium state, a highly stretchable and tough PAA/DODMAC complex hydrogel can be achieved. The hydrogels demonstrate limited swelling in water, probably due to the robust and high-density polyelectrolyte/surfactant complexes formed between oppositely charged surfactants and weakly charged PAA chains. In addition, the resulting hydrogels are all opaque at room temperature (Supplementary Fig. 1), indicating the heterogeneous structure in the network. With AA content increasing, the hydrogels exhibit increased water content and decreased Young's modulus (Supplementary Fig. 2). It is noted that the hydrogel with AA:DODMAC feeding molar ratio of 9:1 exhibits maximum breaking strain and toughness. Considering that the high breaking strain of the hydrogel is beneficial for high-performance actuation of SMPs, we will choose this hydrogel sample for further fabrication of the artificial muscle, which can be simply obtained after air-drying of the PAA/DODMAC complex hydrogel. Electrostatic crosslinking between DODMAC and PAA is a prerequisite for maintaining the structural integrity of the complex in water, whereas the double-tailed hydrophobic architecture is essential for forming crystalline domains and, consequently, for enabling thermo-responsive actuation behavior (Supplementary Fig. 3).

The water-responsive behavior of the artificial muscle is examined by testing the mechanical performance of the PAA/DODMAC complex before and after fully hydration (Fig. 2a). In the dried state, the complex behaves as a rigid plastic with high strength and modulus, whereas fully hydration transformed it into a soft, highly elastic and tough hydrogel. Cyclic loading tests (Fig. 2b, c) demonstrated that the hydrogel maintained an energy dissipation ratio above 70% across various strain levels, confirming efficient energy dissipation via reversible dissociation/reformation of physical interactions. To evaluate the internal interactions in the PAA/DODMAC complex, FTIR spectra of PAA, DODMAC and the dried PAA/DODMAC complex were compared in Fig. 2d. PAA exhibits a characteristic peak at 1700 cm^{-1} corresponding to υ(C = O) of PAA, and the peak at 1475 cm^{-1} for DODMAC is related to υ(C-N^+). For the PAA/DODMAC complex, υ(C-N^+) for DODMAC shifts to lower wavenumber. Meanwhile, a new band appears at 1560 cm^{-1}, which can be assigned to υ(COO^-). Then, we can conclude that the presence of DODMAC will deprotonate COOH groups in PAA chains and form ionic complex with PAA. Furthermore, time-dependent FTIR spectra of the PAA/DODMAC complex hydrogel during air-drying were collected to elucidate the water responsive behavior of molecular interactions in the PAA/DODMAC complex. As shown in Fig. 2e and Supplementary Fig. 4, water evaporation can be confirmed from the apparent intensity decreases of δ(O-H) at 1650 cm^{-1}. Meanwhile, υ(COOH) shifts obviously to higher wavenumbers, indicating the severe dehydration of COOH groups along PAA chains. In contrast, υ(COO^-) only exhibits small shift to lower wavenumbers, suggesting that ionic complexation of COO^-/C-N^+ groups is slightly strengthened after dehydration. Moreover, υ_{as}(CH_2) and υ_s(CH_2), mainly contributed by DODMAC, demonstrates neglected wavenumber shift during air-drying of the hydrogel. Under such a circumstance, it is inferred that the water-responsive behavior of the PAA/DODMAC complex is dominated by hydration/dehydration process of PAA chains.

To gain deeper insight into the water-responsive behavior, we employed low-field (LF) ^{1}H NMR spectroscopy to probe proton mobility in the PAA/DODMAC complex[34–36]. As shown in Fig. 2e, two peaks can be identified in the dried complex, which are related to protons in PAA/DODMAC and absorbed water from low to high T_2 (spin-spin relaxation time), respectively. After fully hydration, both T_2 peaks shift to higher values, indicating protons in the hydrogel are more active than that in the dried state. In addition, it is noted that T_2 values of protons in water is lower than 10 ms, suggesting that water molecules are confined in the hydrogel network. Further 2D LF ^{1}H NMR analysis (Fig. 2g, h) confirms the transition of protons from strong confined to less confined states in the PAA/DODMAC complex during hydration process. Herein, these mobility metrics are closely correlated with the mechanical state of the PAA/DODMAC complex.

The internal structure of the PAA/DODMAC complex has been systematically examined by Small-angle X-ray scattering (SAXS) and wide-angle X-ray scattering (WAXS) methods. Figure 2i displays the SAXS-WAXS results of the PAA/DODMAC complex in the dried and fully hydrated (hydrogel) states. For the hydrogel, the scattering intensity I versus scattering vector q can be divided into two main regions. In the region $q > 0.15$ $Å^{-1}$, the observed scattering peaks correspond to the first-order (around 0.182 $Å^{-1}$) and second-order (around 0.368 $Å^{-1}$) diffraction peaks of the densely packed multi-bilayer lamellar structures of DODMAC complexed with PAA, as well as a coherent peak related to the DODMAC long-chain spacing (around 1.506 $Å^{-1}$)[31]. The elevated scattering in the region $q < 0.15$ $Å^{-1}$ is attributed to PAA clusters within the system. These clusters, with a radius of gyration (R_g) of ~35 Å, connect the multi-bilayer domains and form a loose gel-network structure, with the scattering following a q^{-2} power law. After air-drying, the first-order scattering peak from the stacked PAA/DODMAC bilayer lamellar phase shifts to a higher q value of ~0.192 $Å^{-1}$. This shift corresponds to a decrease in the bilayer spacing from d = 34.5 Å in the fully hydrated gel to 32.7 Å upon dehydration. The result indicates that water loss compresses the inter-bilayer distance, forcing the hydrophobic tails within the bilayers to couple at a smaller tilt angle and leading to a slight reduction in layer spacing. This change is consistent with the shift of the chain-spacing-related peak in the WAXS region from 1.506 $Å^{-1}$ in the hydrogel to 1.523 $Å^{-1}$ in the dried complex (corresponding d values decrease from 4.17 Å to 4.12 Å). Meanwhile, the scattering in the $q < 0.15$ $Å^{-1}$ region changes more significantly. A coherent peak from a dense PAA separated phase appears at ~0.12 $Å^{-1}$ (corresponding phase spacing d_PAA = 52.3 Å). Furthermore, the scattering in the low-q region follows a $q^{-3.4}$ power law, indicating a denser structure compared to the hydrogel. Therefore, the SAXS-WAXS results suggest that dehydration mainly induces the collapse of the loose PAA clusters, which, together with the slight densification of multi-bilayer lamellas.

Thermal-responsive behavior of PAA/DODMAC Complex

Owing to the double-tail structure with two long alkyl chains, DODMAC exhibits a phase transition from a solid-like to a fluid-like state with the disorder of the alkyl chains increasing after heating above 45 °C[32,33], providing a molecular basis for the thermal-responsive behavior of PAA/DODMAC Complex. As shown in Fig. 3a, the PAA/DODMAC complex exhibits a high Young's modulus (E) of 798 MPa and tensile breaking strength (σ_b) of 14 MP at 20 °C, originated from a rigid physical network formed by crystalline microdomains of the hydrophobic DODMAC chains. Upon heating to 60 °C, the complex undergoes a

https://doi.org/10.1038/s41467-026-76899-1

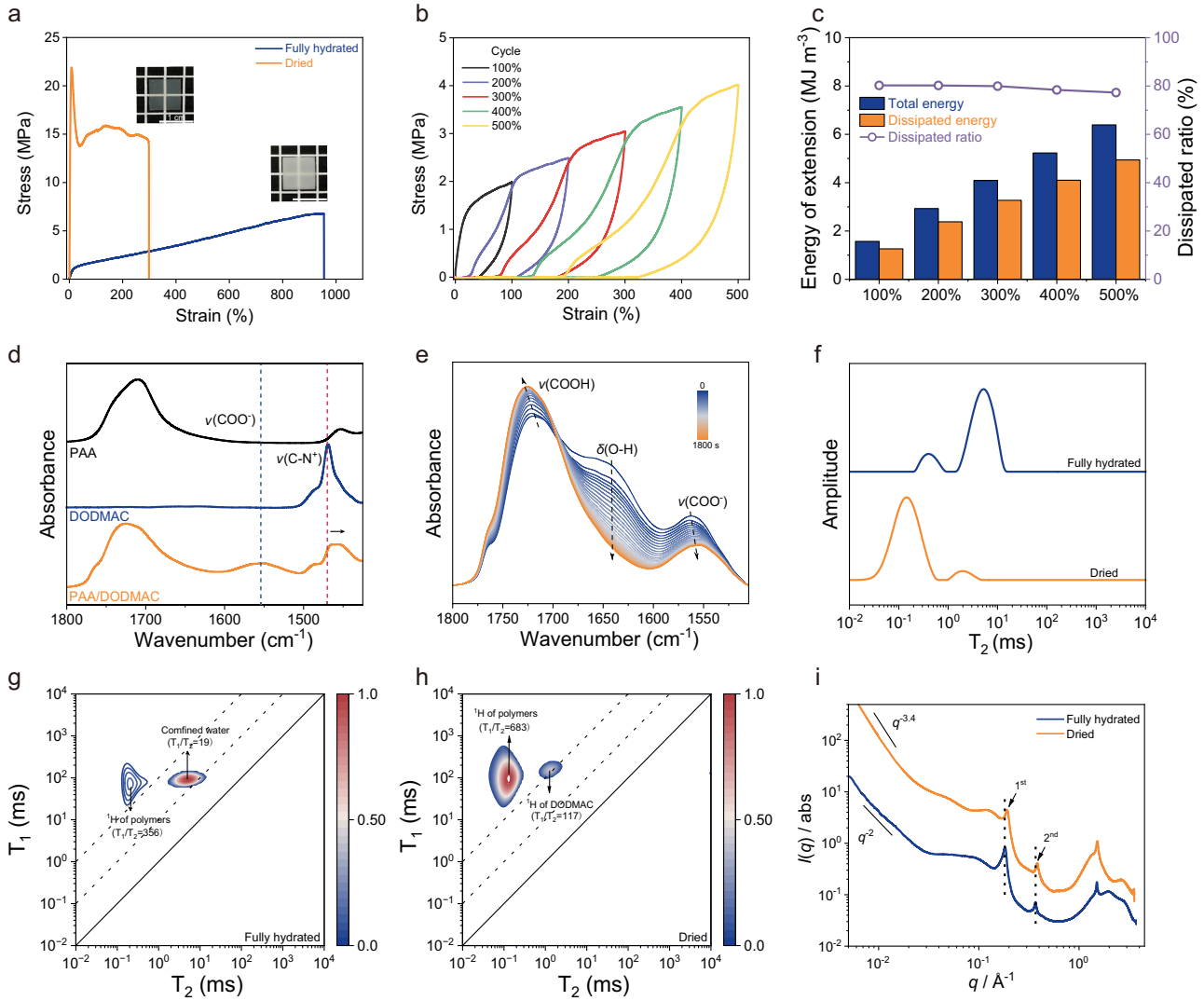


Fig. 2 | Structural basis for water-responsive behavior of PAA/DODMAC. **a** Stress-strain curves and corresponding photographs of the PAA/DODMAC complex before and after hydration. The scale bar is 1 cm. **b** Continuous loading-unloading tensile curves (without intervals) and **c** the corresponding total energy, dissipated energy and dissipation ratio of the fully hydrated PAA/DODMAC complex subjected to varied strains (100–500%). **d** FTIR spectra of PAA, DODMAC and the PAA/DODMAC complex. **e** Time-dependent FTIR spectra of fully hydrated PAA/DODMAC complex during air drying. **f** 1D LF ^{1}H NMR spectra (**f**) and 2D LF ^{1}H NMR T_1/T_2 spectra (**g**, **h**) of the PAA/DODMAC complex in dried and fully hydrated states. **i** SAXS-WAXS profiles of the PAA/DODMAC complex in dried and fully hydrated states.

distinct stiff-to-soft transition with E decreasing to ~62 MPa (Supplementary Fig. 5). In addition, dynamic mechanical analysis (DMA) was performed to examine the mechanical change of the PAA/DODMAC complex under varied temperatures (Fig. 3b). The storage modulus (E') of the complex remains constant below 40 °C and starts to decrease abruptly after heating above 40 °C, confirming the thermal-induced stiffness-switch of the PAA/DODMAC complex. Such a modulus change correlates directly with the melting of crystalline microdomains of alkyl chains, which weakens physical crosslinking and results in lower stiffness. Differential scanning calorimetry (DSC) curves further show a clear endothermic peak at ~42 °C during heating and an exothermic peak at ~20 °C during cooling (Fig. 3c), providing thermodynamic evidence of the reversible phase transition. Meanwhile, the transition temperature is tunable by changing AA-to-DODMAC feed ratio or surfactant alkyl chain length (Supplementary Fig. 6). It is noted that a similar thermal-induced stiffness switch is observed in the fully hydrated PAA/DODMAC complex (Supplementary Fig. 7), which would facilize the processing of artificial muscle fibers in the hydrogel state.

FTIR spectroscopy has been intensively used as a means of investigating phase transitions[37,38]. To elucidate the dynamic molecular mechanism of thermal-responsive behavior of PAA/DODMAC complex, temperature-dependent FTIR spectra of the complex during heating from 20 to 60 °C have been collected, as displayed in Fig. 3d and Supplementary Fig. 6. Herein, we mainly focus on CH stretching region (3000–2820 cm^{-1}) to monitor the changes of DODMAC during the phase transition. For CH groups, mostly contributed by long alky chains of DODMAC, both υ_{as} (CH_2) and υ_s (CH_2) shift to higher wavenumbers during heating, revealing the order-to-disorder transition of alky chains[32,33]. Quantitative analysis on the frequency shifts of CH_2 stretching bands demonstrates a discontinuous increasing at 36 °C (Supplementary Fig. 8), indicating the phase transition occurs at 36 °C from the molecular level. Perturbation-correlation moving window (PCMW) method[39,40], which could correlate external perturbations directly with variations in the spectral bands, providing a powerful way to determine the specific transition points. Figure 3e presents PCMW synchronous and asynchronous spectra of CH stretching region during heating, from which we could deduce that the alky chains of

https://doi.org/10.1038/s41467-026-76899-1

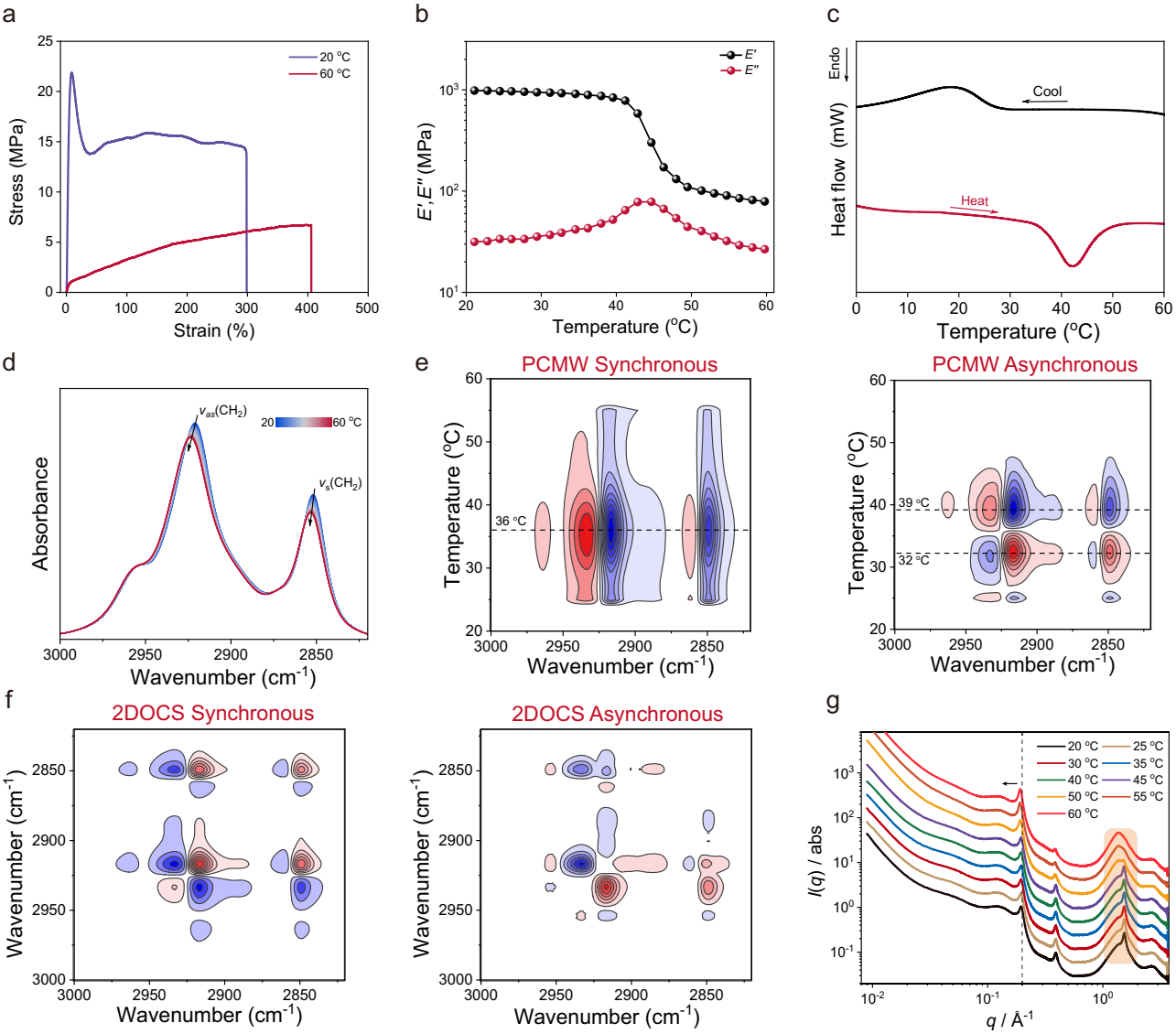


Fig. 3 | Structural basis for thermal-responsive behavior of dried PAA/DODMAC complex. a Tensile stress-strain curves of the PAA/DODMAC complex at 20 and 60 °C. **b** DMA curves showing storage modulus (*E′*) and loss modulus (*E″*) of the PAA/DODMAC complex during heating from 20 to 60 °C. **c** DSC heating and cooling curves of the PAA/DODMAC complex between 0 and 60 °C. **d** Temperature-variable FTIR spectra of PAA/DODMAC complex from 20 to 60 °C. PCMW (**e**) and 2DCOS (**f**) analysis of temperature-variable FTIR spectra of PAA/DODMAC complex. Herein, red and blue represent positive and negative intensities, respectively. **g** Temperature-variable SAXS-WAXS profiles of the PAA/DODMAC complex (20–60 °C).

DODMAC experience phase transition at 36 °C with a transition range of 32 to 39 °C. This value slightly deviates from the DMA and DSC results, which probably originates from: i) variations in temperature measurement between instruments; ii) different thermal sensitivity between microscopic molecular interactions and macroscopic properties. Based on the phase transition evolving regions obtained from PCMW, two-dimensional correlation spectroscopy (2DCOS) analysis was performed with temperature-variable FTIR spectra between 32 and 39 °C to differentiate various CH_2 groups and discern their sequential response during phase transition. In Fig. 3f, subtle bands at 2933, 2916 and 2849 cm^{-1} have been identified in the 2D asynchronous map, which can be related to υ_{as} (CH_2) (disordered), υ_{as} (CH_2) (ordered) and υ_s (CH_2), respectively. According to Noda's rule[41], the sequential events with regard to CH groups during phase transition can determined as follows: 2933 → 2849 → 2916 cm^{-1}, that is, $\upsilon_{as}(CH_2)$ (disordered) → $\upsilon_s(CH_2)$ → $\upsilon_{as}(CH_2)$ (ordered). This sequence highlights that disordered CH_2 groups are more sensitive to temperature rise than ordered ones. Meanwhile, for the $\upsilon(COO^-)$ band, it exhibits neglected variation upon heating, indicating that ionic interactions between COO^- of PAA and $C\text{-}N^+$ of DODMAC remain undisturbed during the phase transition process (Supplementary Fig. 9). Those ionic complexes will act as strong physical crosslinkers in the network and contribute greatly to enhance the actuation performance of the artificial muscle.

Temperature-dependent SAXS-WAXS results in Fig. 3g reveal the structural evolution of the PAA/DODMAC complex between 20 °C and 60 °C. It is shown that the first- and second-order peaks of the PAA/DODMAC complex bilayers exhibit a slight tendency to shift toward lower q with heating, corresponding to a slight increase in bilayer spacing. Meanwhile, the change is more pronounced in the WAXS region, where the sharp scattering peak around 1.531 $Å^{-1}$ almost disappears after heating above 50 °C. It is probably related to the order-disorder transition of the packed alkyl chains of DODMAC. Moreover, the scattering peak at a smaller q value becomes dominant in the WAXS region, indicating that heating also leads to an expansion of the alky chain-spacing. Meanwhile, the low-q scattering from the PAA

https://doi.org/10.1038/s41467-026-76899-1

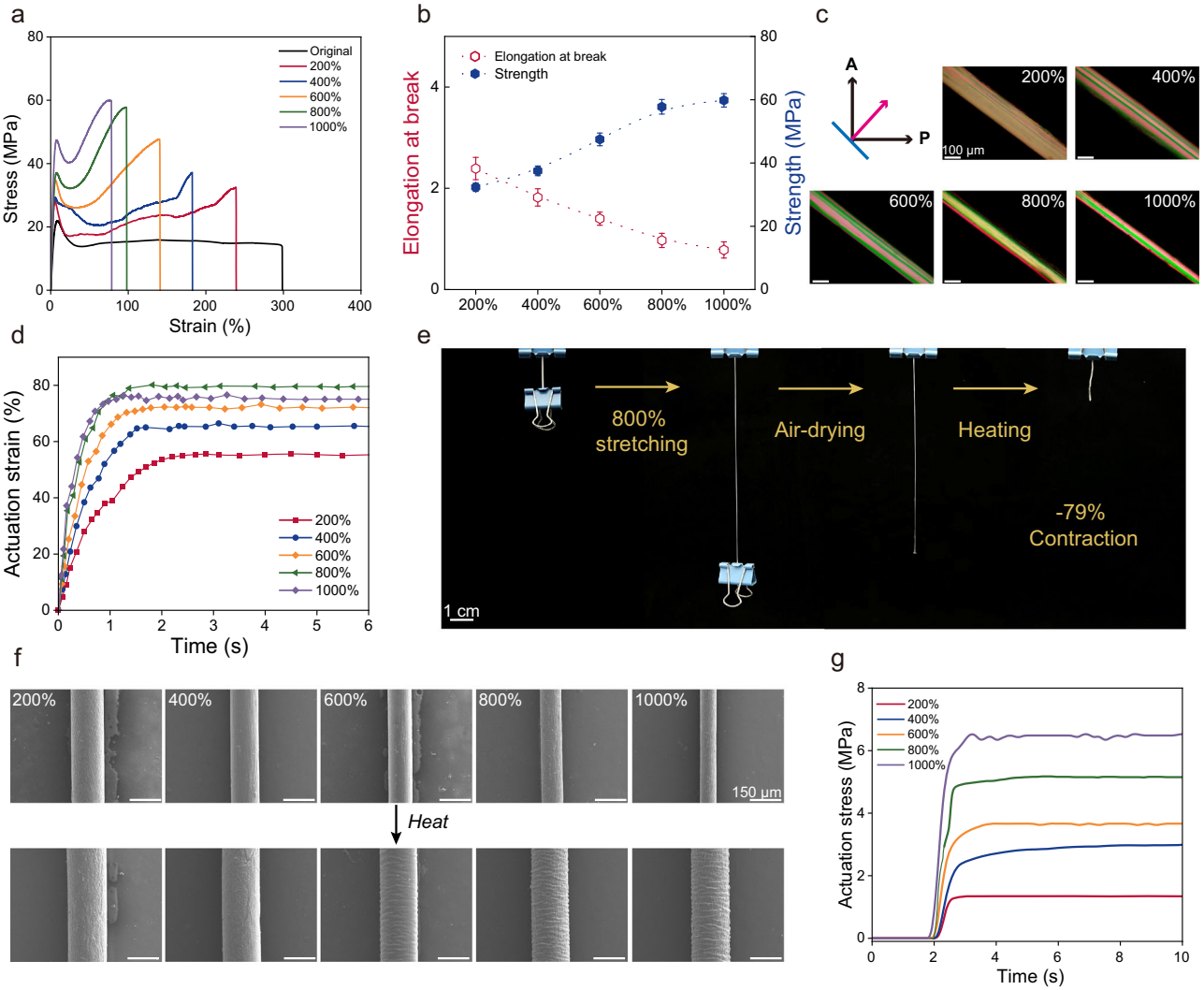


Fig. 4 | PAA/DODMAC complex fiber exhibiting superior mechanical and actuation performance. a Stress-strain curves of fiber with pre-stretching ratios from 200 to 1000%. **b** Comparison of the mechanical properties of fiber with varied pre-stretching ratios. **c** Polarized optical microscopy (POM) images of fiber pre-stretched from 200 to 1000%. **d** Actuation contraction strain of fiber with different pre-stretching ratios upon heating to 45 °C. **e** Photographs of the strain-controlled shape memory process of the fiber with 800% pre-stretching. **f** SEM images before and after actuation for the fiber with varied pre-stretching ratios. **g** Contractile actuation stress generated by 200-1000% pre-stretched fibers under thermal trigger. Data are presented as the mean values ± SD, $n = 3$ independent samples. Source data are provided as a Source Data file.

phase shows no obvious change during heating. Thus, it is revealed that heating mainly disrupts the ordered packing of two long alky chains in the DODMAC.

Artificial muscle fibers demonstrating superior mechanical and actuation properties

Benefited from the water- and thermal-responsive behavior of the PAA/DODMAC complex, we adopted a facile two-step method to fabricate artificial muscle fiber: 1) preparing hydrogel fibers with a pre-oriented structure by uniaxially stretching the fully hydrated PAA/DODMAC complex at 50 °C; 2) air-drying the stretched hydrogel at room temperature. The restored mechanical energy in the stretching fiber is released when DODMAC experience a phase transition of crystalline to liquid-like alkyl chains under mildly heating to 45 °C. Herein, the highly stretchable nature of the PAA/DODMAC hydrogel fibers endows the artificial muscle fiber with high restored entropic energy, thus contributing to the actuation performance. The mechanical properties of the fibers at different stretching ratios (200 to 1000%) were systematically investigated. Uniaxial tensile tests (Fig. 4a) revealed that as the pre-stretch ratio increased, the elongation at break gradually decreased from 240% to 70%, while the tensile strength rose markedly from 32 to 60 MPa (Fig. 4b). The Young's modulus increased from 0.9 GPa to 1.5 GPa (Supplementary Fig. 10). This trend is primarily due to the enhanced alignment of macromolecular chains, which improves load-bearing capacity but simultaneously limits entropic elasticity. All fibers exhibited excellent overall toughness (Supplementary Fig. 11). In addition, the creep of the dry-state fiber is virtually negligible (Supplementary Fig. 12). Polarized optical microscopy (POM) and 2D SAXS were employed to observe the chain orientations in the samples. In Fig. 4c, as the stretching ratio increases, the fiber shows decreased diameter and brighter colors, confirming a highly aligned arrangement of both polymer chains and crystalline microdomains along the stretching direction. In Supplementary Fig. 13, the first-order peak around $q = 0.19$ Å^{-1} and the second-order scattering ring around $q = 0.39$ Å^{-1} become anisotropic with the stretching ratio increasing, suggesting that the bilayer lamellar structures align preferentially along the stretching direction.

The actuation performance of the 200-1000% fibers was evaluated by examining the length change during contraction in the absence of loading. When heated, the fibers contracted significantly,

with the actuation strain and rate depending on the programmed deformation (Fig. 4d). As the programmed elongation ratio increased from 200–1000%, the maximum actuation strain reached 79% with an instantaneous actuation rate as high as 107% s^{-1} (Supplementary Fig. 14). Figure 4e shows a sequence of photographs clearly capturing the complete thermally driven shape recovery of a fiber programmed at 800% elongation. It should be noted that further increasing the elongation ratio to 1000% led to a decline in actuation performance, likely due to excessive alignment, which may reduce the density of effective physical crosslinks and thereby lower the stored entropic energy available for contraction. Wrinkling on the fiber surface became visible under microscopic observation upon heating (Fig. 4f), directly reflecting macroscopic deformation induced by the melting of crystalline domains and chain reorganization. Stepwise heating without load verified the fiber's ability to produce graded displacement, with stable intermediate contraction states at each temperature step, confirming monotonic and continuously tunable actuation (Supplementary Fig. 15).

In addition to shape-change capability, actuation stress is a key parameter for evaluating the actuation performance of artificial muscles[42]. Measurements using a loading frame showed that actuation stress increased with higher programming ratios (Fig. 4g). Specifically, fibers programmed at 1000% generated an actuation stress as high as 6.4 MPa, ~17 times that of natural skeletal muscle. This stress-generation mechanism can be explained by a theoretical model[43] (Supplementary Fig. 16). During stretching, molecular chains and crystalline microdomains become aligned and deformed, storing mechanical energy. Upon heating and melting, entropic recovery and phase transition work together to generate significant contraction stress under macroscopic constraint[44,45].

Work capacity, cyclic stability, and reversible actuation behavior in artificial muscles

The actuation performance of the PAA/DODMAC complex fiber is governed by a stimuli-decoupled mechanism: hydration enables the large pre-stretch programming that sets the actuation strain, dehydration converts the material into a high-modulus network capable of delivering large actuation stress, and thermal triggering releases the stored entropic energy to drive the final actuation output. Acting as an artificial muscle, the PAA/DODMAC complex efficiently converts external thermal energy into mechanical work and exhibits stable, reversible actuation under cyclic loading without external assistance. To directly demonstrate its work capacity, we performed a load-lifting experiment (Fig. 5a and Supplementary, Movie 1), where the stretched PAA/DODMAC complex fiber was fixed at one end and attached to a weight at the other to apply constant stress. When heated above the phase transition temperature (~ 42 °C), the fiber contracted rapidly and lifted the weight, demonstrating direct thermal-to-mechanical energy conversion. The PAA/DODMAC complex also demonstrated its potential as a stable and rapid-response actuator. When heated, an 800% pre-stretched PAA/DODMAC fiber readily drives a cart carrying a payload. (Supplementary, Movie 2).

We further quantified the dependence of actuation performance on applied stress (Fig. 5b and Supplementary Fig. 17). As the external stress increased, the maximum actuation strain decreased from ~80% to about 5%, since part of the driving energy is consumed to overcome the external load. Despite this reduction in strain, the work density (work per unit mass) initially increased with stress, reaching a peak of about 181 $J{\cdot}kg^{-1}$ at around 1.5 MPa, ~four times that of natural skeletal muscle. This peak-shaped stress–work relationship is characteristic of efficient actuators. At low stress, large strain is achieved, but the output force is limited; at high stress, the output force increases, but the strain becomes too small. The PAA/DODMAC complex fiber exhibits a relatively broad peak range, indicating its adaptability to different loading conditions while maintaining efficient energy output. We further characterized the frequency response of actuation strain and work density under constant load (Fig. 5c). Within 0.02-5 Hz, the strain amplitude decayed gradually with increasing frequency, indicating the frequency dependence of the actuation behavior (Supplementary Fig. 18). To enable broader applications, the high-frequency actuation performance of this thermomechanical artificial muscle still needs to be optimized.

Different from common SMP-based artificial muscles, the PAA/DODMAC complex fiber can be facilely re-programmed under extreme stimuli of heat and water, providing excellent stress-controlled reversible actuation. After thermally induced contraction, the load-bear fiber can be re-stretched after hydration at 45 °C and then dried to fix its temporary shape. Upon reheating, it contracts and lifts the attached weight (Fig. 5d). It is noted that Figs. 1, 5d illustrate the same load-bearing actuation process, in which the load remains attached throughout both drying and heating. In contrast, Fig. 4e depicts the load-free actuation process, where the load is removed prior to heating to demonstrate the intrinsic shape memory capability of the material. The actuation strain can be precisely tuned by the programming stress: increasing the load raised the pre-stretch strain from 30% to 500%, while the thermal contraction strain reached a maximum of about 18% under a 10 g load (Fig. 5e). Cyclic actuation tests under constant stress demonstrated outstanding repeatability (Fig. 5f). Over ten complete cycles, the actuation and recovery strains remained highly consistent, confirming the fatigue resistance of the dynamic physical network under repeated phase transition and entropic recovery. The strong electrostatic interactions between PAA and DODMAC maintain network integrity under prolonged water immersion, as evidenced by stable swelling and fully retained DODMAC content over ten hydration-actuation cycles without detectable leakage. (Supplementary Fig. 19). We also characterized reversible actuation under fixed length (isometric conditions). A pre-stretched fiber was clamped at both ends and subjected to periodic heating, during which melting of crystalline microdomains converted entropic contraction tendency into internal stress (Fig. 5g and Supplementary Fig. 20). The 800% fiber generated highly reversible contraction stress with stable peak values and baseline over more than 50 cycles, showing no performance degradation. This ability to reversibly produce and release stress at a fixed length mimics the isometric contraction of biological muscles, offering potential for applications such as micro-grippers[46] and adaptive dampers[47]. Beyond the direct heating method, photothermal conversion and conductive coatings can also be introduced to broaden the application scenarios of this artificial muscle[48]. Compared with previously reported artificial muscles, our system addresses the typical trade-off between high actuation stress and large actuation strain under mild conditions (Supplementary Fig. 21 and Supplementary Table 1). Under isometric conditions, the peak actuation stress reached 6.4 MPa; under load-free conditions, the maximum strain was 79%; and at an applied stress of ~1.5 MPa, the peak work density was 181 $J{\cdot}kg^{-1}$. Given that these values are obtained under different actuation modes, a clear understanding of the respective testing conditions is essential for a comprehensive performance evaluation.

Discussion

In summary, we successfully develop a phase separated PAA/DODMAC complex that overcomes key challenges in artificial muscle design, specifically, the trade-off between high actuation stress and high strain, as well as the need for mild activation and intrinsic reversibility. By ingeniously integrating a thermal-responsive double-tail quaternary ammonium surfactant with a water-responsive hydrophilic network through hierarchical structural engineering, stimuli-decoupled actuation performance is achieved: the dry state provides high actuation stress via strong ionic crosslinking, while the hydrated state offers exceptional stretchability for actuation strain. Thermal triggering around 42 °C, close to body temperature, allows for safe and practical

https://doi.org/10.1038/s41467-026-76899-1

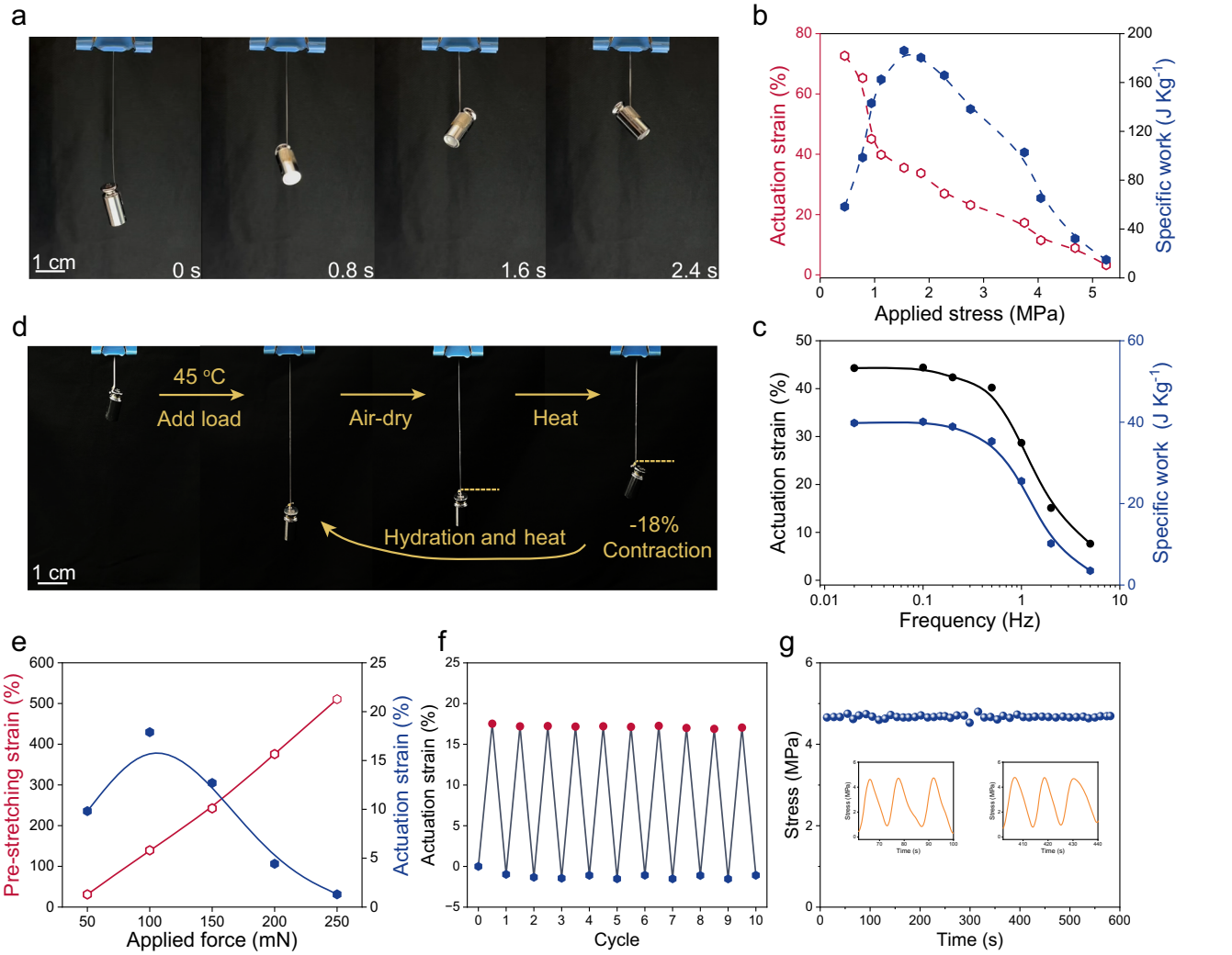


Fig. 5 | Efficient performance and reversible actuation of PAA/DODMAC complex fiber. a Photographs of the load-bearing actuation of the fiber. **b** Actuation strain and work capacity of the fiber with different applied stress. **c** Dependence of contractile strain and power density on thermal cycling frequency under constant load. **d** Photographs of stress-controlled reversible shape memory cycle of the fiber. **e** Pre-stretching strain and corresponding actuation strain of the fiber under varied loads. **f** Actuation stability of the fiber under constant stress. **g** Reversible actuation performance of pre-stretched fiber at fixed length through cyclic heating-cooling.

actuation. Moreover, the dynamic physical network ensures robust fatigue resistance and repeatable self-reversible actuation over multiple cycles without external force. The resulting PAA/DODMAC complex fibers demonstrate performance metrics, including work density (~4× natural muscle) and stress output (~18× natural muscle), that surpass most existing systems. This work provides a scalable material platform that uniquely combines low-temperature actuation, two-way reversibility, and facile reprogrammability, offering a versatile strategy for designing high-performance soft actuators.

Methods

Materials

Acrylic acid (AA, Aladdin), dioctadecyl dimethyl ammonium chloride (DODMAC, 97%, MACKLIN Chemical), 2-hydroxy-2-methylpropiophenone (Irgacure 1173, Aladdin), Unless otherwise mentioned, all chemicals were used as received without further purification or modification.

Preparation of PAA/DODMAC complex

Firstly, AA, DODMAC and H_2O were mixed under stirring at the desired molar ratio. Specifically, molar ratios of AA, DODMAC and H_2O were 45:15:40, 48:12:40, 51:9:40, 54:6:40, 57:3:40, respectively. The photoinitiator 1173 (0.1 mol% relative to the total monomers) was then added to the precursor solution under continuous stirring. The well-mixed solution was purged with N_2 for 20 min and injected into a customized glass mold with ≈0.5 mm thick spacers. UV-initiated polymerization (365 nm, 100 W) was carried out at 50 °C for 0.5 h to obtain the hydrogel. Then, the prepared hydrogel was immersed in a large volume of deionized water to remove residual acrylic acid, DODMAC, and counterions. The water was refreshed daily, and the swelling process was maintained for one week to reach an equilibrium. Finally, the hydrogel was air-dried for three days until a constant weight was achieved, yielding the PAA/DODMAC complex. For PAA/DODMAC complex fibers, the polymerization process was conducted in a glass tube (1 mm × 100 mm).

Characterizations

Surface morphology was examined by scanning electron microscopy (SEM, Hitachi Regulus 8230) with an accelerating voltage of 5 kV. The melting temperature was determined by differential scanning calorimetry (DSC, TA Q250) under a nitrogen atmosphere, with a heating rate of 10 °C min^{-1} over a temperature range of 10–70 °C. DMA tests were conducted using a TA Q800 instrument equipped with a

mechanical cooling accessory, over a temperature range of 20 to 60 °C. Polarized light microscopy (POM) observations were performed using an Olympus BX53-P polarizing microscope.

Small-angle X-ray scattering (SAXS)/wide-angle X-ray scattering (WAXS)

SAXS/WAXS measurements were conducted using the laboratory SAXS-WAXS beamline KWS-X (XENOCS XUESS 3.0 XL) at JCNS-MLZ in Garching, Germany. The Metal Jet X-ray source (Excillum D2 +) was operated with a liquid-metal anode at 70 kV and 3.57 mA, generating Ga-Kα radiation with a wavelength λ = 1.314 Å. The gel samples were loaded into sealed capillaries (inner diameter: 2 mm) and placed on a temperature-controlled stage. Dry gel sample were measured directly in vacuum on the stage. The sample-to-detector distance was varied between 0.12 m and 1.7 m. The SAXS patterns were normalized to an absolute scale, azimuthally averaged to obtain intensity profiles, and subsequently corrected by subtracting the solvent background.

Low-field (LF) 1H-NMR measurements

LF NMR measurements were conducted using a VTMR20-010V-I NMR analyzer (Suzhou Niumag Corporation, China). Two-dimensional (2D) LF-NMR analyses were performed employing a T_1/T_2 correlation pulse sequence based on the inversion recovery Carr-Purcell-Meiboom-Gill (IR-CPMG) method.

Temperature-dependent FTIR measurements

Temperature-variable FTIR spectra of the samples were acquired in transmission mode using a Nicolet iS50 FTIR spectrometer. The samples were placed on the zinc selenide (ZnSe) and subjected to controlled heating from 20 to 60 °C at a constant rate of 1 °C min^{-1}, with spectral collection at 1 °C intervals.

Two-dimensional correlation spectroscopy (2DCOS)

2DCOS analysis was conducted using the software 2D Shige version 1.3 (© Shigeaki Morita, Kwansei Gakuin University, Japan, 2004–2005). The resulting 2DCOS spectra were subsequently visualized as contour plots using OriginPro software. In the generated contour maps, positive correlation intensities are represented in red, while negative correlation intensities are denoted in blue.

Actuation strain experiments

We quantified the actuation strain of the complex fibers through video analysis. For load-free actuation strain measurements, the air-dried complex fiber tip was used as a tracking marker. After calibrating the length scale in the video frames, the initial position of the marker was set as the coordinate origin, and subsequent frame-by-frame analysis was performed to calculate the displacement. For load-carrying actuation strain measurements, the counterweight suspended from the fiber tip was used as the tracking marker, and the same video analysis method was employed to record its position changes during the actuation process. The specific work output (W, J/Kg) can then be calculated by the following equation:

$$W = \frac{m_1}{m_a} gd \tag{1}$$

where m_1 is the load mass, m_a is the fiber actuator mass, d is the displacement, and g is the acceleration of gravity.

Actuation stress experiments

Both ends of the air-dried PAA/DODMAC complex fiber were fixed onto the sample holder of a tensile testing machine under constant strain. The fiber was then heated using a heat gun, and the force readings from the load cell were continuously recorded. The measured force was subsequently converted into stress based on the initial cross-sectional area of the fiber. Each sample was independently measured three times.

Dependence of actuation strain and work capacity on applied stress

The stress applied to the complex fiber was varied by changing the weight of the suspended load. The actuation strain at different stress levels was recorded, and the actuation strain and work capacity of the fiber were calculated and compared accordingly to evaluate the stress dependence of both parameters.

Strain self-actuation experiments

In this type of experiment, the load was always fixed at the end of the composite fiber, and the entire actuation process relied solely on the material's own deformation to lift the load, without any external intervention. The actuation performance of the composite fiber under different loads was evaluated by varying the weight of the load. Specifically, we recorded the pre-stretch strain generated by the hydrogel fiber under its own load, as well as the final actuation strain achieved after heating.

Cyclic strain self-actuation experiments

After completing one actuation cycle, the complex fiber was rehydrated to restore it to its initial hydrogel state, after which the strain self-actuation experiment was repeated. This process was repeated for ten cycles, and the final actuation strain of each cycle was recorded to evaluate the stability of the material properties.

Cyclic stress self-actuation experiments

In this experiment, under conditions of fixed fiber length, stress output was achieved by partially melting the crystalline regions through heating. By precisely controlling the heating temperature and duration, we demonstrated that the complex fiber could generate reversible contractile stress. To verify its long-term stability, we continuously ran over 50 actuation cycles, which showed no degradation in performance.

Tensile testing

Uniaxial tensile tests were performed using a universal testing machine (Shenzhen Sun Technology UTM2103) at a constant strain rate of 0.1 s^{-1} until fracture. Three measurements were conducted for each sample. The elastic modulus was estimated from the slope of the initial linear region of the stress-strain curve. The tensile toughness was calculated as the area under the tensile stress-strain curve. For continuous loading-unloading tests, a speed of 0.1 s^{-1} was employed.

Measurement of mass change rate

After actuation, the PAA/DODMAC complex fibers with known dry mass were immersed in deionized water for full rehydration. Upon reaching swelling equilibrium, the fibers were taken out and weighed to obtain their wet mass. As shown in the added Figure S15, to examine the leakage of DODMAC during repeated hydration cycles, the same fiber was sequentially subjected to pre-stretching, drying, actuation, and rehydration treatments for a total of ten cycles. The dry mass of the fiber after the first actuation (M_0) was used as the reference. The wet mass of the fiber after each swelling equilibrium was recorded as M, and the swelling behavior of the material was evaluated by calculating the mass change.

Creep test

The dry-state fiber was equilibrated at the test temperature for 5 min using dynamic mechanical analyzer (DMA). Subsequently, a constant tensile stress of 500 kPa was applied for 20 min. After the loading period, the stress was removed, and the sample was allowed to recover

at the same temperature for 30 min. The change in strain over time was measured and recorded throughout the entire process.

Statistics and reproducibility

All experiments were repeated independently with similar results at least three times.

Data availability

All data supporting the findings of this study are available within this article and Supplementary Information or from the corresponding author upon request. The data generated in this study are provided in the Supplementary Information/Source Data file. Source data are provided with this paper.

References

1. Liu, H. et al. Multimodal actuation and precise control in liquid crystal elastomer optical fiber artificial muscles. *Adv. Mater.* **37**, e05776 (2025).
2. Hu, W., Lum, G. Z., Mastrangeli, M. & Sitti, M. Small-scale soft-bodied robot with multimodal locomotion. *Nature* **554**, 81–85 (2018).
3. Wang, W. et al. Harnessing the hygroscopic and biofluorescent behaviors of genetically tractable microbial cells to design biohybrid wearables. *Sci. Adv.* **3**, e1601984 (2017).
4. Qiu P.-F. et al. A soft, ultra-tough and multifunctional artificial muscle for volumetric muscle loss treatment. *Natl. Sci. Rev.* **12**, nwae422 (2024).
5. Xia, Y., He, Y., Zhang, F., Liu, Y. & Leng, J. A review of shape memory polymers and composites: mechanisms, materials, and applications. *Adv. Mater.* **33**, 2000713 (2021).
6. Wang, X. et al. Freestanding 3D mesostructures, functional devices, and shape-programmable systems based on mechanically induced assembly with shape memory polymers. *Adv. Mater.* **31**, 1805615 (2019).
7. Li, C. et al. Enabling ultra-high work capacity and scalable processability of liquid crystal actuators through densely entangled structures. *Adv. Mater.* **38**, e13876 (2026).
8. Shi, X. et al. Semiseparated biphasic bicontinuous dielectric elastomer for high-performance artificial muscle. *Science* **390**, 1044–1049 (2025).
9. Dong, L. et al. Elastic-sheathed artificial muscle fibers delivering natural muscle-like resilient actuation for robotics and wearables. *Matter* **8**, 102281 (2025).
10. Cui, Y. et al. Hydration programmable, shape memorable artificial muscles for antagonistic movements. *Adv. Funct. Mater.* **34**, 2401005 (2024).
11. Lang, C. et al. Nanostructured block copolymer muscles. *Nat. Nanotechnol.* **17**, 752–758 (2022).
12. Chen, J. et al. Ultra-highly stiff and tough shape memory polyurea with unprecedented energy density by precise slight cross-linking. *Adv. Mater.* **36**, 2401178 (2024).
13. Guo, Y. et al. Haptic artificial muscle skin for extended reality. *Sci. Adv.* **10**, eadr1765 (2024).
14. Chu, H. et al. Unipolar stroke, electroosmotic pump carbon nanotube yarn muscles. *Science* **371**, 494–498 (2021).
15. Cui, B. et al. Pretension-free and self-recoverable coiled artificial muscle fibers with powerful cyclic work capability. *ACS Nano* **17**, 12809–12819 (2023).
16. Kim, I. H. et al. Human-muscle-inspired single fibre actuator with reversible percolation. *Nat. Nanotechnol.* **17**, 1198–1205 (2022).
17. Wang, X. et al. Knittable electrochemical yarn muscle for morphing textiles. *ACS Nano* **18**, 9500–9510 (2024).
18. Tu, Z. et al. Biomimetic high performance artificial muscle built on sacrificial coordination network and mechanical training process. *Nat. Commun.* **12**, 2916 (2021).
19. Yan, D. et al. Carbon nanotube-directed 7 GPa heterocyclic aramid fiber and its application in artificial muscles. *Adv. Mater.* **36**, 2306129 (2024).
20. Zhao, Q., Qi, H. J. & Xie, T. Recent progress in shape memory polymer: New behavior, enabling materials, and mechanistic understanding. *Prog. Polym. Sci.* **49**, 79–120 (2015).
21. Lendlein, A. & Gould, O. E. C. Reprogrammable recovery and actuation behaviour of shape-memory polymers. *Nat. Rev. Mater.* **4**, 116–133 (2019).
22. Kong, Q. et al. Mimosa-inspired body temperature-responsive shape memory polymer networks: high energy densities and multi-recyclability. *Adv. Sci.* **11**, 2407596 (2024).
23. Ping, Z. et al. Tailoring photoweldable shape memory polyurethane with intrinsic photothermal / fluorescence via engineering metal-phenolic systems. *Adv. Funct. Mater.* **34**, 2402592 (2024).
24. Cui, Y., Li, D., Gong, C. & Chang, C. Bioinspired shape memory hydrogel artificial muscles driven by solvents. *ACS Nano* **15**, 13712–13720 (2021).
25. Li, M. et al. Wet-spinning carbon nanotube/shape memory polymer composite fibers with high actuation stress and predesigned shape change. *Adv. Sci.* **11**, 2404913 (2024).
26. Kong, W., Zhao, X. & Ye, L. A Novel Polyoxymethylene Fiber-Based Artificial Muscle Enabled Stable Actuating Behavior. *Small* **21**, 2502065 (2025).
27. Steck, J., Kim, J., Kutsovsky, Y. & Suo, Z. Multiscale stress deconcentration amplifies fatigue resistance of rubber. *Nature* **624**, 303–308 (2023).
28. Wang, R. et al. Multilayer assembly of dielectric actuators based on a reversibly crosslinkable silicone elastomer. *Adv. Funct. Mater.* **36**, e09974 (2026).
29. Jin, B. et al. Programming a crystalline shape memory polymer network with thermo- and photo-reversible bonds toward a single-component soft robot. *Sci. Adv.* **4**, eaao3865 (2018).
30. Kang, D. et al. Two-way shape memory alloy and polymer composite hybrid smart actuator with high speed, accuracy, and reversible deformation. *Adv. Funct. Mater.* **36**, e28863 (2026).
31. Gonçalves, R. A., Lindman, B., Miguel, M. G., Iwata, T. & Lam, Y. M. Elucidating the effect of additives on the alkyl chain packing of a double tail cationic surfactant. *J. Colloid Interf. Sci.* **528**, 400–409 (2018).
32. Laughlin, R. G., Munyon, R. L., Burns, J. L., Coffindaffer, T. W. & Talmon, Y. Physical science of the dioctadecyldimethylammonium chloride-water system. 3. Colloidal aspects. *J. Phys. Chem.* **96**, 374–383 (1992).
33. Laughlin, R. G., Munyon, R. L., Fu, Y. C. & Fehl, A. J. Physical science of the dioctadecyl dimethyl ammonium chloride-water system. 1. equilibrium phase behavior. *J. Phys. Chem.* **94**, 2546–2552 (1990).
34. Liu, Z., Sun, S. & Wu, P. Water-activated self-adhesion in ultrastrong hydrogel microfibers for smart capturing. *CCS Chem.* **0**, 1–12 (2026).
35. Li, X., Wu, B., Hou, L. & Wu, P. Water-mediated phase separation evolution toward mechanically robust yet room-temperature reprocessable polymer materials. *Matter* **8**, 102099 (2025).
36. Ma, X., Wu, B., Hou, L. & Wu, P. Edible structurally colored plastics. *ACS Nano* **19**, 23945–23954 (2025).
37. Xu, J., Wu, B., Hou, L. & Wu, P. Hydrogen bonding competition mediated phase separation with abnormal moisture-induced stiffness boosting. *Small* **20**, 2401164 (2024).
38. Li, X., Wu, B., Sun, S. & Wu, P. Making sticky-slippery switchable fluorogels through self-adaptive bicontinuous phase separation. *Adv. Mater.* **36**, 2411273 (2024).
39. Sun, S. -t & Wu, P. -y Spectral insights into microdynamics of thermoresponsive polymers from the perspective of two-dimensional correlation spectroscopy. *Chin. J. Polym. Sci.* **35**, 700–712 (2017).

40. Morita, S., Shinzawa, H., Noda, I. & Ozaki, Y. Perturbation-correlation moving-window two-dimensional correlation spectroscopy. *Appl. Spectrosc.* **60**, 398–406 (2006).
41. Noda, I. et al. Generalized two-dimensional correlation method applicable to infrared, raman, and other types of spectroscopy. *Appl. Spectrosc.* **47**, 1329–1336 (1993).
42. Hu, X. et al. Fast and strong carbon nanotube yarn artificial muscles by electro-osmotic pump. *ACS Nano* **18**, 428–435 (2024).
43. Mirvakili, S. M. & Hunter, I. W. Artificial muscles: mechanisms, applications, and challenges. *Adv. Mater.* **30**, 1704407 (2018).
44. Hu, J., Zhu, Y., Huang, H. & Lu, J. Recent advances in shape–memory polymers: Structure, mechanism, functionality, modeling and applications. *Prog. Polym. Sci.* **37**, 1720–1763 (2012).
45. Bai, C. et al. Low-entropy-penalty elastomers with synergistic resilience and strength via resilin-inspired microphase separation. *Adv. Funct. Mater.* **35**, e10053 (2025).
46. Shi, Z. et al. Ultrasound-driven programmable artificial muscles. *Nature* **646**, 1096–1104 (2025).
47. Yang, X. et al. Amplification of integrated microscopic motions of high-density [2]rotaxanes in mechanically interlocked networks. *Nat. Commun.* **13**, 6654 (2022).
48. Fu, J. et al. Large stroke radially oriented MXene composite fiber tensile artificial muscles. *Sci. Adv.* **11**, eadt1560 (2025).

Acknowledgements

The authors gratefully acknowledge the financial support from the National Natural Science Foundation of China (Nos. 52573130 and 52433003) and the Natural Science Foundation of Shanghai Basic Research Funding (No. 25ZR1401006).

Author contributions

H.L. carried out most experiments and co-wrote the manuscript. L.H. and P.W. supervised the project and co-wrote the manuscript. B. W. analyzed the SAXS results. All authors discussed the results and revised the manuscript.

Funding

L. H. discloses support for the research of this work from the the National Natural Science Foundation of China (No. 52573130) and the Natural Science Foundation of Shanghai Basic Research Funding (No. 25ZR1401006). P. W. discloses support for the research of this work from the the National Natural Science Foundation of China (No. 52433003).

Competing interests

The authors declare no competing interests.

Additional information

Supplementary information The online version contains supplementary material available at https://doi.org/10.1038/s41467-026-76899-1.

Correspondence and requests for materials should be addressed to Lei Hou or Peiyi Wu.

Peer review information *Nature Communications* thanks the anonymous reviewers for their contribution to the peer review of this work. A peer review file is available.

Reprints and permissions information is available at http://www.nature.com/reprints

Publisher's note Springer Nature remains neutral with regard to jurisdictional claims in published maps and institutional affiliations.

Open Access This article is licensed under a Creative Commons Attribution-NonCommercial-NoDerivatives 4.0 International License, which permits any non-commercial use, sharing, distribution and reproduction in any medium or format, as long as you give appropriate credit to the original author(s) and the source, provide a link to the Creative Commons licence, and indicate if you modified the licensed material. You do not have permission under this licence to share adapted material derived from this article or parts of it. The images or other third party material in this article are included in the article's Creative Commons licence, unless indicated otherwise in a credit line to the material. If material is not included in the article's Creative Commons licence and your intended use is not permitted by statutory regulation or exceeds the permitted use, you will need to obtain permission directly from the copyright holder. To view a copy of this licence, visit http://creativecommons.org/licenses/by-nc-nd/4.0/.

© The Author(s) 2026